A digital-based approach for characterising spread powder layer in additive manufacturing

Yi He *, Jabbar Gardy, Ali Hassanpour, Andrew E. Bayly

School of Chemical and Process Engineering, University of Leeds, Leeds, United Kingdom

HIGHLIGHTS

- A general approach to characterise spread powder layer based on space discretization.
- Qualitative and quantitative evaluations enabled for packing density, surface profile and pores.
- Density pore for less populated area and chamber pore for size of empty patch.
- Sensitivity tests conducted on sampling parameters.
- Applicability demonstrated for simulation-generated and experimentally spread powder layers.

GRAPHICAL ABSTRACT
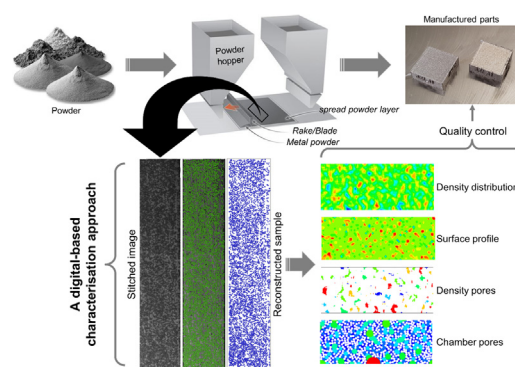
ARTICLE INFO

ABSTRACT

Assessing the quality of a spread powder layer is critical to understanding powder spreadability in additive manufacturing. However, the small layer thickness presents a great challenge for a systematic and consistent characterisation of the spread powder layer. In this study, a novel digital-based characterisation approach is proposed based on space discretization, with an emphasis on the characteristics that is important to powder-bed-based additive manufacturing. With the developed approach, the spread powder layer can be qualitatively illustrated by contour maps and quantified by statistics of packing density, surface profile and pore characteristics. For the first time, two types of pores are proposed for the spread powder layer. The density pore can identify those less populated areas while the chamber pore is able to quantify the size of empty patches observed in the spread powder bed. Applicability of this approach is demonstrated via both simulation-generated and experimentally spread powder layers. Sensitivity tests on the sampling parameters are conducted. This digital-based characterisation method is general and can be applied to both polydisperse and non-spherical particle systems, not only enriching detailed structural analysis of the spread powder layer but also allowing us to quantitatively evaluate powder spreadability in additive manufacturing.

1. Introduction

Additive manufacturing (AM) has shown its promise in fast prototyping of near-net-shape structures in many applications, such as aerospace, automotive, medical and energy storage industries [1,2].

In powder-bed-based AM processes, material deposition is often achieved via powder spreading (or recoating) using a blade, rake or rotating roller. A thin layer of powder is spread onto a substrate prior to material consolidation in selective regions using either a high intensity energy source (e.g. laser, electron beam or plasma) or a binder [3,4]. The structural, mechanical, and thermal properties of final fabricated parts are found to be strongly correlated with the quality of spreading [4–7]. Considerable efforts have thus been made to develop a better

* Corresponding author.
E-mail addresses: y.he1@leeds.ac.uk (Y. He), A.E.Bayly@leeds.ac.uk (A.E. Bayly).

understanding of the factors affecting the homogeneity of a spread powder layer via both modelling [8–15] and experiments [16–18]. However, a systematic approach to assess the quality of a spread powder layer is still lacking, making it difficult to achieve quantitative understanding and hence process optimisation of powder spreading.

Characterisation of an assembly of particulate material can be made either from a macroscopic viewpoint or using local structural descriptors. Packing density (or porosity) is an important global quantity which relates closely to local packing structure. Many empirical or semi-empirical models have therefore been developed to describe the relationship between packing density and particle characteristics [19,20]. In recent years, experimental techniques [21,22] and numerical simulations have been increasingly used to reveal packing structure and consequently leading to the development of statistical descriptions of local parameters, such as the radial and angular distribution functions [23], orientational orders [22], coordination number and neighbour number [20]. More detailed structural information can be obtained by geometrical tessellations, such as Voronoi tessellation [24,25] or navigation map (an extension of Voronoi tessellation to polydisperse systems) [26]. Particularly, Voronoi tessellation can effectively characterise both particle and pore networks, allowing us to model transport properties or to build-up statistical mechanics theory for particle packing [27]. These approaches have been successfully applied to systems consisting of mono-sized [20] and polydisperse [28], spherical and non-spherical [25], coarse and fine [23,29], friction and frictionless [28] particles. However, these methods could not be applied to a spread powder layer without modification, as the small layer thickness may introduce large uncertainties to the calculation of local cell volumes. Moreover, at present it remains difficult to accurately capture the positions of fine particles within a spread powder layer using the conventional experimental methods. For example, the commonly used optical imaging systems may only able to provide reliable data on a single-layered powder layer, although no results have been reported yet. X-ray tomography is a possible solution for multi-layered spread powder bed but an in-situ spreading rig is required. With the rapid increase of computational powder, discrete element modelling (DEM) has become an indispensable alternative, as it provides detailed information at particle scale. It has been applied to study the influence of material properties, such as particle size [9], shape [13] and cohesion [10,14], and operational conditions, such as blade clearance [10,30], spreading speed [10,12], coater type [11–13,30,31] and gas-particle interaction [32,33] on the quality of spread layer. However, to date, characterisations of a spread powder layer are largely limited to the packing density and surface profiles, which limits the quantitative information that can be extracted. To the best of our knowledge, detailed pore characteristics of a spread powder layer have yet to be reported, although it is related to some key properties of an additively fabricated part, such as permeability, sintering behaviour, and mechanical strength.

The available experimental methods for pore size distribution analysis are either based on absorption of fluids, such as nitrogen, carbon dioxide, helium, water and mercury, or radiation, such as optical microscope, focused ion beam, scanning/transmission electron microscope, X-ray tomography and nuclear magnetic resonance with different magnifications. These methods are usually applicable for bulk materials and thus remain challenging to extract pore information of a spread powder layer. The difficulty in determining pore characteristics of a thin powder layer lies in at least two aspects: firstly, particles involved in AM processes are of small size and in large quantities, which is computationally demanding for both simulations and experiments to accurately track the position of particles; secondly, the small layer thickness makes it difficult to apply existing definitions of three-dimensional pores and consequently a consistent characterisation approach is lacking. For example, Sweeney and Martin [34] proposed a digital-based approach for DEM-simulated powder compacts and thereby both throat pore and chamber pore can be characterised. However, large error can be anticipated when applying this approach to a thin spread powder layer due to variations of surface profiles across the spread powder layer. Recently, Nan et al. [8] presented a method to counting the appearance of empty patches in a numerical sample obtained by DEM simulation, where the spread powder layer was divided into several consecutive bins. An empty patch is identified when the packing density of a bin is smaller than a threshold value (i.e. 0.1). It should be noted here, however, that although their method captures the existence of the local empty patches, it lacks the quantitative information on the pore characteristics, for example, size, shape, and orientation of these pores.

In this study, a digital-based characterisation approach is developed by discretising working space into voxels, which provides a basis for extracting both qualitative and quantitative metrics from a spread powder layer. For the first time, two types of pores of relevance to additive manufacturing are proposed, with their calculation procedures detailed. The so-called density pore allows less populated regions to be identified and characterised in terms of size, shape, and orientation while the chamber pore quantitatively evaluate the size of empty patches observed in a spread powder layer. The applicability of this approach is first demonstrated on a simulation-simulated spread powder layers. Sensitivity tests are then carried out, aiming to provide guidance on the selection of sampling parameters. Combined with imaging analysis, this approach is also demonstrated to be useful for extracting structural information from an experimentally spread powder layer. The rest of the paper is structured as follows: a detailed description of the digital-based approach is first presented in Section 2. This is followed by a brief description of DEM approach and simulation conditions in Section 3. In Section 4, sensitivity tests are carried out on a DEM-simulated spread powder layer. Application of the proposed method to experimentally spread powder layer is shown in Section 5.

2. A digital-based characterisation method

The proposed characterisation method is based on space discretisation, which allows the quality of a spread powder layer to be assessed in terms of packing density, surface roughness and pore characteristics. For a given spread powder layer (either from simulations or experiments), the working space is first discretised into voxels, with voxel size denoted as Δ_{voxel}. Voxels located within particles are then labelled as solid voxels (v_s) while those outside of particles are labelled as void voxels (v_e).

2.1. Packing density and surface roughness

Both packing density and surface roughness are sampled with the aid of a 2D Cartesian grid. The grid size is denoted as Δ_{grid}, which determines the spatial density of sampling points. At each grid node, local structural information is calculated using a local sampling domain. A smaller grid size is thus expected to provide more data points. For simplicity, the local sampling domain has a square-shaped base with its dimension determined by a local sampling size (Δ_s for the sampling of local packing density and Δ_r for local surface height), as schematically illustrated in Fig. 1(a).

A gap-based packing density is introduced here, as a ratio of particle volume to the volume of local sampling domain,

$$\phi_{ij} = \frac{1}{\Delta_s^2 h} \sum_{ip \in \Omega_{ij}} V_{ip} \tag{1}$$

where V_{ip} is the volume of particle ip that located within the local sampling domain Ω_{ij}. The sampling height h is set same as the blade clearance (i.e. $h = h_b$) rather than the actual layer thickness. This is because the actual layer thickness may vary with particle properties and process parameters and it may be even larger than the blade clearance under certain circumstances. A gap-based packing density thus enables a consistent comparison among different cases and is also able to
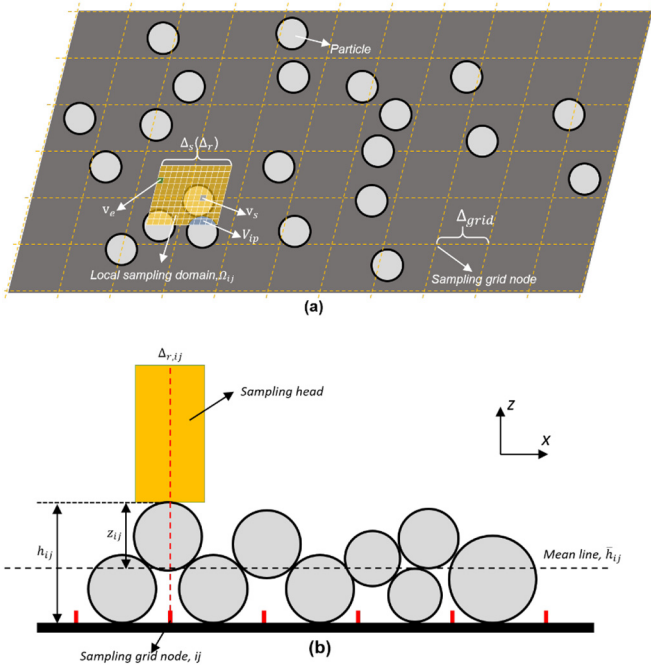
Fig. 1. The schematics of sampling (a) packing density and (b) surface profile.

$$h_{ij} = \max_{v_s \in \Omega_{ij}} h(v_s) \tag{3}$$

where $h(v_s)$ is the vertical height of a solid voxel v_s. This calculation approach allows a pure surface characterisation of a spread powder layer to be made, which mimics the experimental approach of measuring surface profile using a probe of size Δ_r. The mean line can then be calculated from the raw profile data as,

$$\bar{h}_{ij} = \frac{1}{n} \sum_{i=1}^{n} h_{ij} \tag{4}$$

where n is the total number of nodes of the sampling grid. Vertical deviation from the mean line can be given as,

$$z_{ij} = h_{ij} - \bar{h}_{ij} \tag{5}$$

The arithmetical mean deviation (or surface roughness) R_a can then be calculated as,

$$R_a = \frac{1}{n} \sum_{i=1}^{n} |z_{ij}| \tag{6}$$

2.2. Density pore

Powder spreading is often aimed at producing a thin and densely packed powder layer with high uniformity. An uneven spread powder layer can lead to processing issues due to variations in the dynamics of laser-material interactions [7]. It is thus of interest to identify and to characterise those less populated regions in a spread powder layer. As shown in Fig. 2, a so-called density pore is introduced (i.e. the red region in Fig. 2(b)) by thresholding the contour map of local packing density (Fig. 2(a)), in which the pixel size is same as the grid size used to sample local packing densities (i.e. Δ_{grid}).

The coordinates of each pixel can be represented by a vector, $\mathbf{x}_i = [x_i \; y_i]^T$, where T refers to transpose operation. The resulting pore region can be defined by a mass density function $f(\mathbf{x}_i)$ so that $f(\mathbf{x}_i) = 1$ for pixels within the pore while $f(\mathbf{x}_i) = 0$ for pixels outside of it. Fig. 2(c) shows the identified boundary pixel of the density pore. Quantitative feature of density pore, such as size, shape, and orientation, can then be obtained by calculating moments of the filtered pore region. For

quantify the mass per unit area being deposited on the build plate. Instead of calculating it analytically, as particles may be truncated by the local sampling domain, the gap-based local packing density is simply determined as a ratio of the number of solid voxels to the total number of voxels within the local sampling domain Ω_{ij}, i.e.,

$$\phi_{ij} = \sum_{v \in \Omega_{ij}} [v = v_s] / \sum_{v \in \Omega_{ij}} [v] \tag{2}$$

where Ω_{ij} is the local sampling domain at grid node ij. $[\ldots]$ is the Iverson bracket, $[P] = 1$ if P is true, and $[P] = 0$ if P is false.

Surface homogeneity can be evaluated by measuring surface profile across the spread powder bed. As shown in Fig. 1(b), at a given grid node ij, local surface height is determined by the maximum vertical coordinate (i.e. z-coordinate) of solid voxels found within the local sampling domain (Ω_{ij}), i.e.,

Fig. 2. (a) Contour map of local packing density, (b) identification of the region of density pore, in which pixel in the red-coloured region has a local packing density ϕ smaller than 0.1 and (c) identified boundary of density pore. (For interpretation of the references to colour in this figure legend, the reader is referred to the web version of this article.)

a 2D region, the pqth moments regarding to its centroid can be calculated as,

$$\mu_{pq} = \sum_{i=1}^{n} (x_i - \overline{x})^p (y_i - \overline{y})^q f(x, y) \tag{7}$$

where $[\overline{x} \quad \overline{y}]^T$ gives the centroid of the pore. The area of a pore can be simply calculated by counting the number of pixels within the pore region, namely the zeroth moment (μ_{00}). In the present study, the size of density pore is defined as its equivalent circular area diameter (i.e. the diameter of a circle of same area as the pore region) while its orientation is defined by its major axis (i.e. the axis about which the moment of inertia is minimised), which can be calculated by constructing its covariance matrix, i.e.,

$$\mathbf{C} = \frac{1}{\mu_{00}} \begin{bmatrix} \mu_{20} & \mu_{11} \\ \mu_{11} & \mu_{02} \end{bmatrix} \tag{8}$$

which is basically the inertia moment tensor of a pore region. The diagonal elements of the inertia moment tensor are the principal moments of inertia while the off-diagonal elements are the products of inertia, which captures the resistance to rotational forces about the axes. The angle θ of the major axis can be calculated as,

$$\theta = \frac{1}{2} \tan^{-1} \left(\frac{2\mu_{11}}{\mu_{20} - \mu_{02}} \right) \tag{9}$$

The shape of the density pore can be characterised by its circularity, given as,

$$\kappa = \frac{4\pi A}{P^2} \tag{10}$$

where A is the area of a pore region and P is the perimeter of the pore region. $\kappa = 1$ means a circular pore shape. The smaller the circularity, the more elongated the pore shape is.

2.3. Chamber pore

Mechanical strength of an AM fabricated part relates closely to its internal pore structure, knowledge on the pore structure in the spread powder layer is thus also desired. However, due to a small layer thickness, the conventional definition of three-dimensional pores is not applicable for a thin powder layer. The variation of surface profile could lead to large error in determining local pore volumes. Instead of quantifying internal pore structure, this study adapts the concept of chamber pore to quantify the size of two-dimensional empty patches (or voids) observed in a spread powder layer. The calculation procedure is outlined below.

Particles are first projected onto a sampling plane paralleled to the spread powder bed, resulting in a 2-D image as shown in Fig. 3(a). This is achieved by discretising the whole working space and the sampling plane into voxels and pixels, respectively. Those voxels occupied
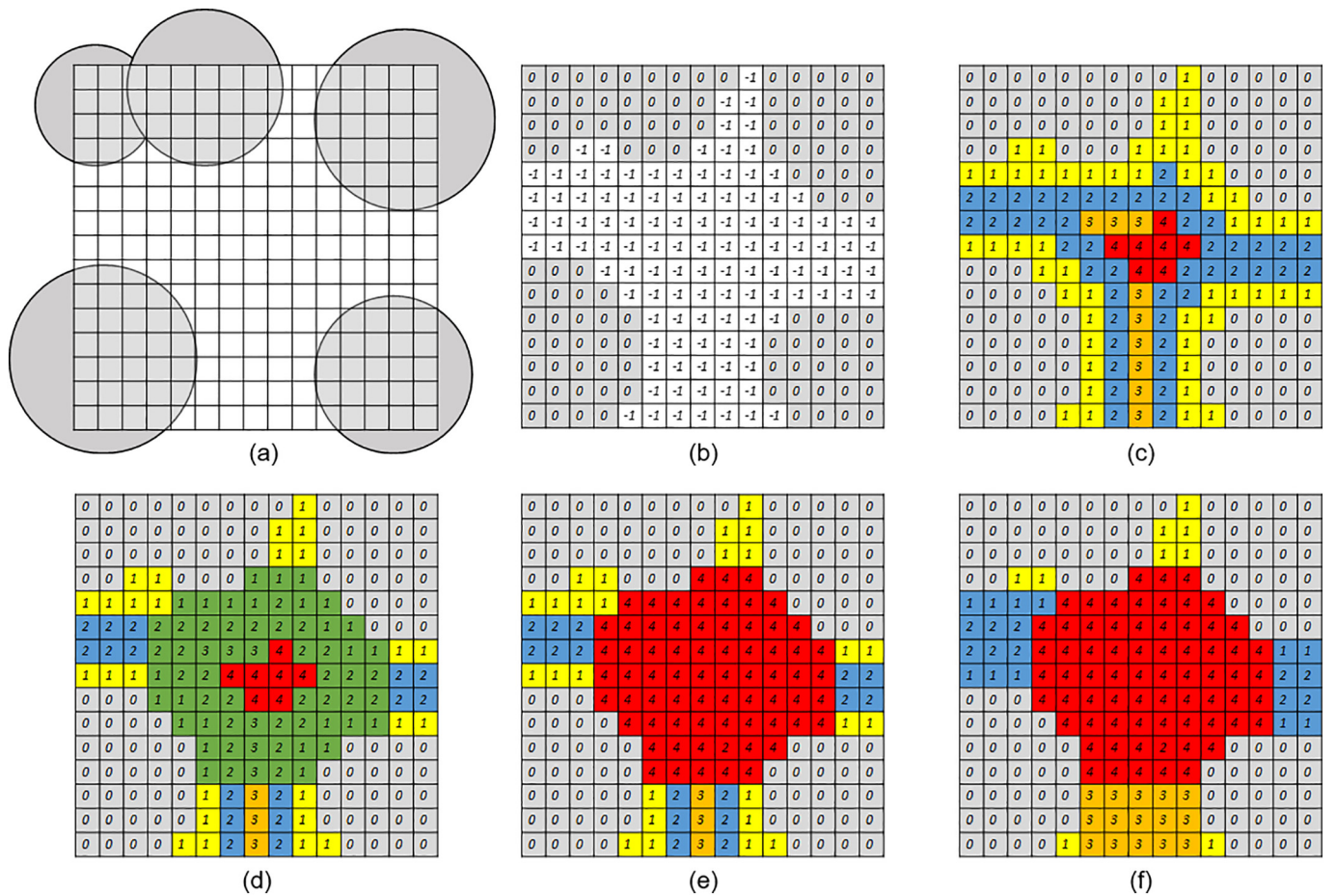
Fig. 3. Determination of chamber pores: (a) schematics of solid particles and sampling grid, (b) project particles onto the sampling plane, labelling pixels occupied by particles as "0" and those of voids as "-1"; (c) Each void pixel is labelled according to its distance to the nearest solid pixel, with its value determined as $\lceil d/\Delta_{pixel} \rceil$, where d is the distance and Δ_{pixel} is the pixel size; (d) the neighbouring pore pixels located in a circle of radius smaller than 4-pixel length are shaded as green; (e) The layer number of these shaded pixels are adjusted to 4 and (f) the resulting pore space. (For interpretation of the references to colour in this figure legend, the reader is referred to the web version of this article.)

by particles are labelled as solid voxels. Iteration over the voxels is then performed in the vertical direction from the top to bottom. If a solid voxel is found, the corresponding pixel on the sampling plane is labelled as '0' while those of voids are labelled as '-1'. The resulting pixel status is illustrated in Fig. 3(b). Then, each pore pixel is marked according to its distance to the nearest solid pixel (referred as layer number), with its value determined as $[d/\Delta_{pixel}]$ where d is the distance between two pixels and Δ_{pixel} is the pixel size, as shown in Fig. 3(c). Once the shortest distance between pore pixel and solid pixel is found, the pore pixel of the largest integer number is chosen. The neighbouring pixels are then examined to see if the distance to the selected pixel is less than the layer number. Taking the pore pixels with the layer number of 4 as an example, the neighbouring pore pixels located in a circle of radius smaller than 4-pixel length are shaded as green (Fig. 3(d)). Finally, the layer number of these shaded pixels are adjusted to the value of 4 (i.e., the radius of the largest circle that can be enclosed in the pore space), as shown in Fig. 3(e). This step will be re-iterated until there are no pore pixels left to be adjusted, the resulting pore space is illustrated in Fig. 3(f). Finally, the distribution of chamber pore size can be obtained by simply counting the number of pixels of each integer value. It should be noted this method is also applicable to systems of different particle shapes and sizes.

3. Numerical models and simulation conditions

The developed characterisation approach is first applied to a spread layer of cohesive fine powder generated by DEM modelling. The DEM models are detailed in previous studies [35–38] and thus is only briefly outlined here. For a particle of radius R_i, mass m_I and moment of inertia I_I, the resulting governing equations can be written as,

$$m_i \frac{d\mathbf{v}_i}{dt} = \sum_j \left(\mathbf{F}_{cn,ij} + \mathbf{F}_{dn,ij} + \mathbf{F}_{ct,ij} + \mathbf{F}_{dt,ij} \right) + \sum_k \mathbf{F}_{v,ik} + m_i \mathbf{g} \tag{11}$$

$$I_i \frac{d\boldsymbol{\omega}_i}{dt} = \sum_j \left(\mathbf{r}_{ij} \times \mathbf{F}_{t,ij} + \mu_r |\mathbf{F}_{cn,ij}| \boldsymbol{\omega}_i/|\boldsymbol{\omega}_i| \right) \tag{12}$$

where $\mathbf{v}_i$ and $\boldsymbol{\omega}_i$ are the translational and rotational velocities, respectively. $\mathbf{F}_{cn, ij}$ and $\mathbf{F}_{dn, ij}$ are the normal contact force and normal damping force while $\mathbf{F}_{ct, ij}$ and $\mathbf{F}_{dt, ij}$ are the frictional force and the damping force in the tangential direction. The torques acting on the particle consists of a torque due to the tangential forces and a rolling resistance torque due to the asymmetric distribution of the contact pressure, where μ_r is the rolling friction coefficient. The Hertz-Mindlin theory [39] is adopted to calculate the contact forces. The van der Waals force ($\mathbf{F}_{v, ik}$) between two particles is governed by the Hamaker theory [40]. These force models are summaries as follows,

$$\mathbf{F}_{cn,ij} = \frac{4}{3} E^* R^{*1/2} \delta_n^{3/2} \hat{\mathbf{n}} \tag{13}$$

$$\mathbf{F}_{dn,ij} = 2\sqrt{\frac{5}{6}} \beta_n \sqrt{S_n m^*} \mathbf{v}_{ij}^n \tag{14}$$

$$\mathbf{F}_{ct,ij} = \begin{cases} -\mu_t |\mathbf{F}_{cn,ij}| \left[1 - (1 - |\boldsymbol{\delta}_t|/\delta_{t,\max})^{3/2} \right] \hat{\boldsymbol{\delta}}_t & |\boldsymbol{\delta}_t| < \delta_{t,\max} \\ -\mu_t |\mathbf{F}_{cn,ij}| \hat{\mathbf{v}}_t & |\boldsymbol{\delta}_t| \geq \delta_{t,\max} \end{cases} \tag{15}$$

$$\mathbf{F}_{d,t} = 2\sqrt{\frac{5}{6}} \beta_t \sqrt{S_t m^*} \mathbf{v}_{ij}^t \tag{16}$$

$$\mathbf{F}_{v,ik} = \begin{cases} \dfrac{AR^*}{6 s_{\min}^2} \hat{\mathbf{n}} & s < s_{\min} \\ \dfrac{AR^*}{6 s^2} \hat{\mathbf{n}} & s_{\min} \leq s \leq s_{\max} \\ 0 & s \geq s_{\max} \end{cases} \tag{17}$$

where the effective radius R^* is given by $R^* = R_i R_j/(R_i + R_j)$ and the reduced mass is calculated as $m^* = m_i m_j/(m_i + m_j)$. The effective elastic modulus E^* is calculated as $1/E^* = (1 - \nu_i^2)/Y_i + (1 - \nu_j^2)/Y_j$, with Y_i being the Young's modulus and ν_i the Poisson's ratio of particle i. In the calculation of damping forces, $S_n = 2E^* \sqrt{R^* \delta_n}$ and $S_t = 8G^* \sqrt{R^* \delta_n}$, with G^* the effective shear modulus and δ_n the magnitude of the normal overlap. $\delta_{t, \max} = \mu_t \delta_n (2 - \nu)/(2 - 2\nu)$ is the critical tangential displacement. In the van der Waals force model (i.e. Eq. (17)), s is the interparticle separation distance and A is the Hamaker constant. $s_{\min}$ is a cut-off surface separation, below which the van der Waals force is assumed to be constant. $s_{\max}$ is the maximum cut-off distance for van der Waals interaction introduced to save computational cost, as the force magnitude drops dramatically with increasing surface separation.

The simulation was conducted in a rectangular box, with periodic boundary conditions applied to both the front and the rear sides of the box. As shown in Fig. 4, one complete simulation consists of three stages: die filling, heaping, and spreading. A rigid blade is used as an example of coating device. The blade is initially located at the left side of the box while a gate is located $40d_p$ in front of the blade. Particles are initially generated randomly within the confined space formed by the blade and the front gate. This is followed by a gravitational setting process to form a stable packing, with the gravity acting in the vertical direction. After that, the front gate is removed, a stable heap is formed in front of the blade. Finally, the blade spreader is lifted to a certain height (i.e. 75 μm) and a constant speed is given for spreading (i.e. 50 mm/s). It should be noted that although a single layer of powder spreading is modelled here, spreading powder on a previously solidified bed can be modelled by calibrating interfacial energy, surface profile, sliding and rolling friction between particle and the substrate.
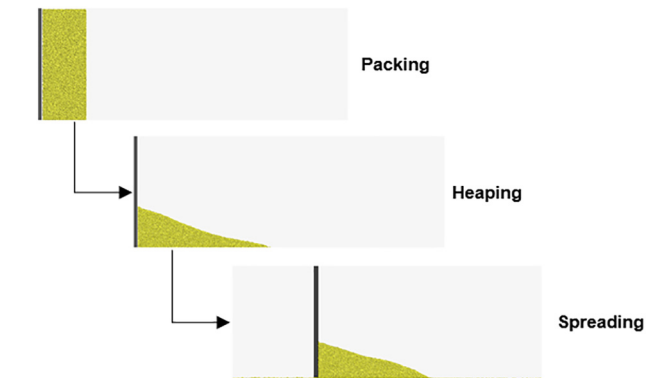
Fig. 4. Three stages of simulating powder spreading, from particle packing to heaping and spreading.

Table 1
Parameters used in the present simulation.

Parameter	Value
Particle number	100,000
Particle diameter, d_p (μm)	50
Density, ρ (kg/m^3)	4430
Young's modulus, E (GPa)	110
Poisson ratio, ν	0.3
Sliding friction coefficient, μ_s	0.3
Rolling friction coefficient, μ_r	0.01
Restitution coefficient, e	0.4
Hamaker constant, A (J)	1.86×10^{-22}
minimum cut-off distance, $s_{\min}$ (m)	1.65×10^{-10}
Blade gap, h_b (μm)	75
Blade thickness, δ_b (μm)	200
Blade speed, v_b (mm/s)	50

Table 2
Simulation configuration for the sampling of packing density.

Case	Voxel size (d_p)	Sampling size (d_p)	Sampling grid size (d_p)
1	0.05	2, 3.0, 4.0, 5.0	1.0
2	0.025–0.2	3.0	1.0
3	0.05	3.0	0.25, 0.5, 1.0, 2.0

Table 3
Simulation configuration for the sampling of surface profile.

Case	Voxel size (d_p)	Sampling head size (d_p)	Sampling grid size (d_p)
4	0.05	0.5, 1.0, 1.5, 2.0	1.0

Table 4
Simulation configuration for the sampling of density pores.

Case	Density threshold	Sampling size (d_p)	Sampling grid size (d_p)
5	0.1	2.0, 3.0, 4.0, 5.0	0.1
6	0.06, 0.08, 0.1, 0.12	3.0	0.1

Table 5
Simulation configuration for the sampling of chamber pores.

Case	Pixel size (d_p)
7	0.1, 0.05 (*base*), 0.025, 0.0125

In the present study, a newly developed stiffness-independent DEM approach is applied to model cohesive fine powders in spreading. Details of the approach can be found in our previous paper [35]. Simulations were performed using an in-house, GPU-based DEM code (**HiPPS**) which has been extensively used in the modelling of different particulate systems, such as particle packing [36], compaction [37,38] and fluid-particle interactions [41,42]. Noting that quantitative experimental validation on spreading is not aimed here, but instead focus is given to the information that can be extracted by the proposed digital-based characterisation approach. Table 1 lists the parameters used in the simulation, where the particle properties of a typical Ti-6Al-4V powder are used. The minimum cut-off distance s_{min} is the same as that used in the study of Parteli and Pöschel [43]. For simplicity of discussion, mono-sized particles of size 50 μm were used in the study.

Tables 2–5 list the simulation configurations of sensitivity tests for data sampling. Effects of voxel size, local sampling size and grid size on the resulting density distributions are examined. Local sampling size determines the area from which local packing density is calculated while grid size controls the number of sampling points to be collected. Noting that sampling height is the same as the blade gap (i.e. $1.5d_p$) for the calculation of local packing density. For surface profile, focus is given to the effect of local sampling size. For density pores, effects of density threshold value, local sampling size and sampling grid size are examined while keeping voxel size constant as $0.05d_p$. The setup of case 5 is essentially the same as that of the case 1, from which the density pores are identified by a density threshold of 0.1. For the sampling of chamber pores, the effect of pixel size is examined.

4. Results and discussion

4.1. Packing density

4.1.1. Effect of local sampling size

Fig. 5 shows the top view of spread powder layer from DEM simulation and the resulting distributions of local packing density. Here, the whole space is discretised using a voxel size of $0.05d_p$. Local packing density is sampled on a grid with a grid size of $1.0d_p$. Four different local sampling sizes are used to calculate local packing density at each grid node: $2d_p$, $3d_p$, $4d_p$ and $5d_p$. The sampling height is the same as the blade gap (i.e. $1.5d_p$). Sampling size is shown to have an influence
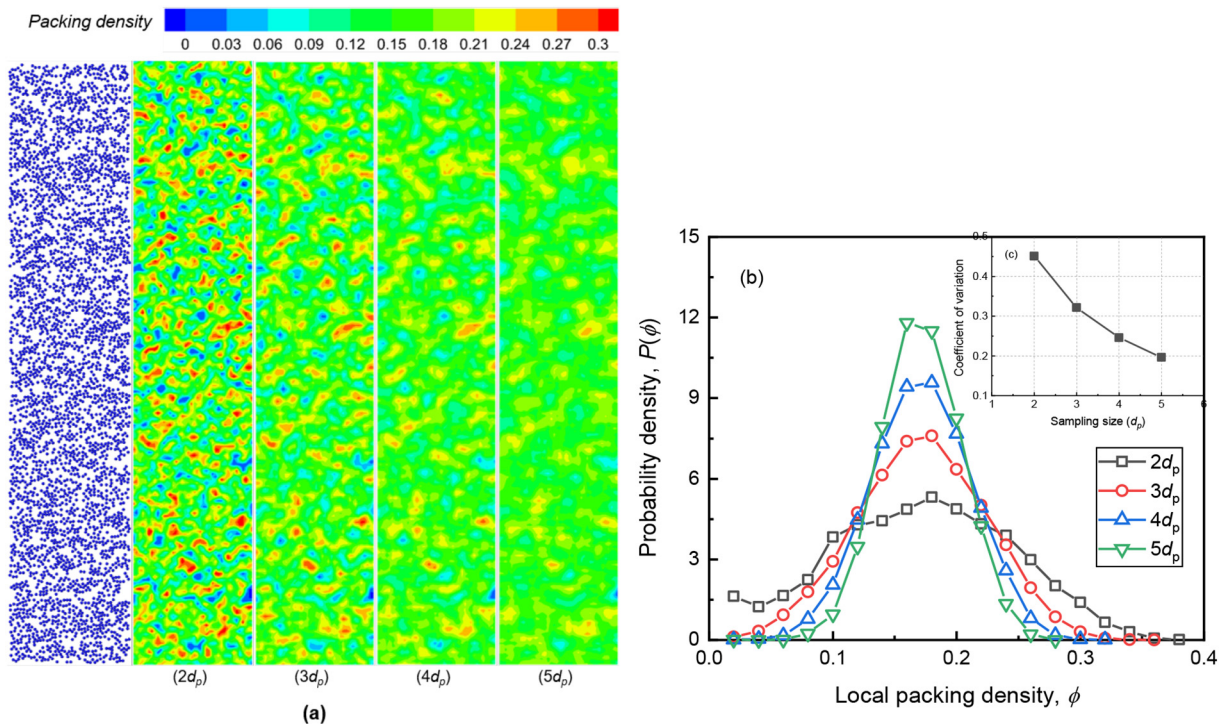
Fig. 5. (a) Top view of the spread powder bed and contour maps of local packing density calculated using different sampling sizes, (b) Effect of sampling size on statistical distribution of packing density.
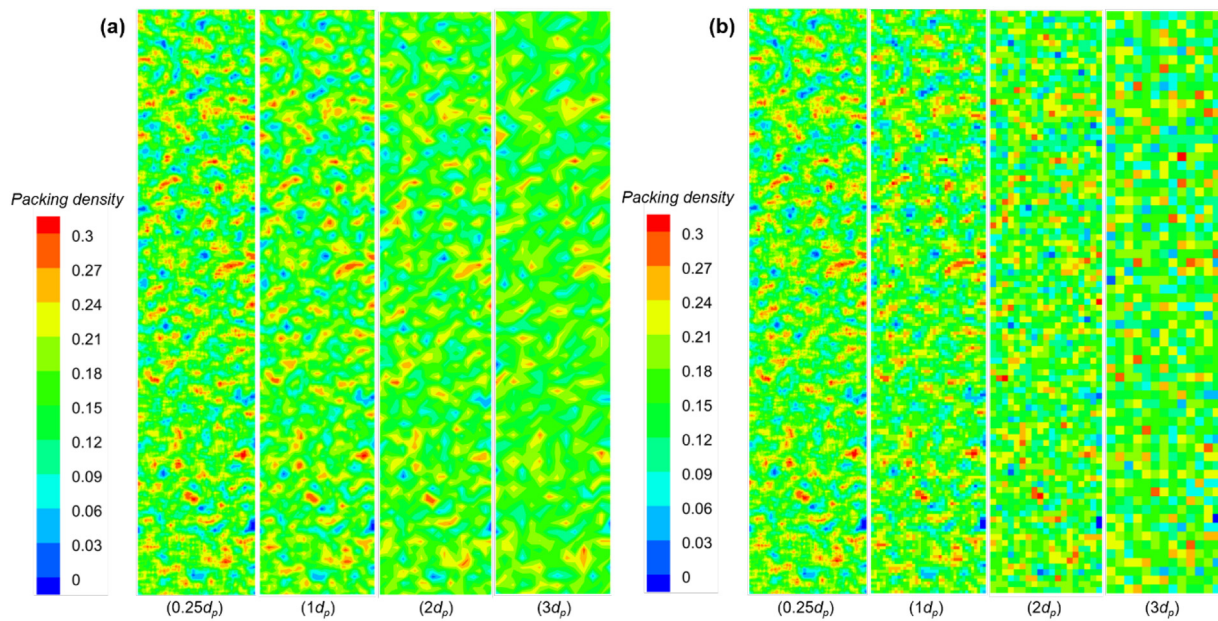
Fig. 6. Effects of sampling grid size on spatial distribution of packing density, in which (a) linear interpolation is applied and (b) without any interpolation, only cell-entered data is shown.

on the homogeneity of the density maps. Local features, such as empty patches, is more pronounced with a smaller sampling size. This is mainly because a large sampling size tends to smear out local gradients in the density distribution. Qualitatively, it suggests that a sampling size larger than $3d_p$ is not suitable, as the local empty patches cannot be represented clearly in the density map. This is also confirmed by the statistical distribution of local packing density, as shown in Fig. 5(b). With an increasing sampling size, the distribution becomes narrower, but with an increasing peak value at the mode which remains almost constant. Consequently, the calculated coefficient of variation which represents homogeneity of the spread layer is increased with a larger sampling size. The presence of empty patches can only be reflected clearly in the statistical distribution with a sampling size of $2d_p$, which also indicates that the majority of empty patches have a size smaller than $3d_p$. The sampling size thus has little influence on the mean packing density but strongly affects variation of the sampled packing density and hence should be selected based on the problems of interest. For example, for selective laser melting, it should be smaller than the spot size of laser

as structural variations on smaller scales can be largely homogenised by dynamics of molten pool [9].

4.1.2. Effect of grid size

Grid size determines the total number of data points to be sampled. A smaller grid size corresponds to a larger number of data points. It is thus of interest to identify the maximum allowable grid size to minimise computational expense. Four different grid sizes are examined here: $0.25d_p$, $1d_p$, $2d_p$ and $3d_p$, with constant local sampling size (i.e. $3.0d_p$) and voxel size (i.e. $0.1d_p$). Fig. 6 shows the sampled contour maps of packing density with and without linear interpolation. The interpolation shows little influence for a grid size smaller than $1.0d_p$ while significant difference can be observed for $2.0d_p$ and $3.0d_p$. A grid size smaller than the local sampling size is thus required to provide sufficient data points.

The upper bound of grid size can be further elucidated from statistics of packing density. As shown in Fig. 7(a), the mean value of packing density remains relatively stable up to a grid size of $2.0d_p$, with a relative
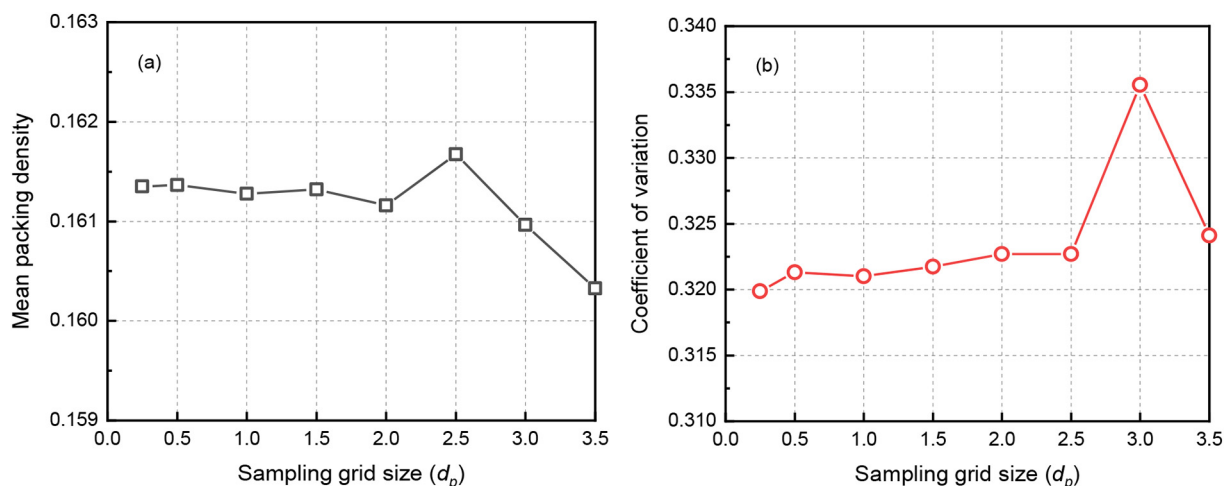
Fig. 7. Effects of sampling grid size on the average packing density, in which (a) mean packing density and (b) coefficient of variation of packing density.
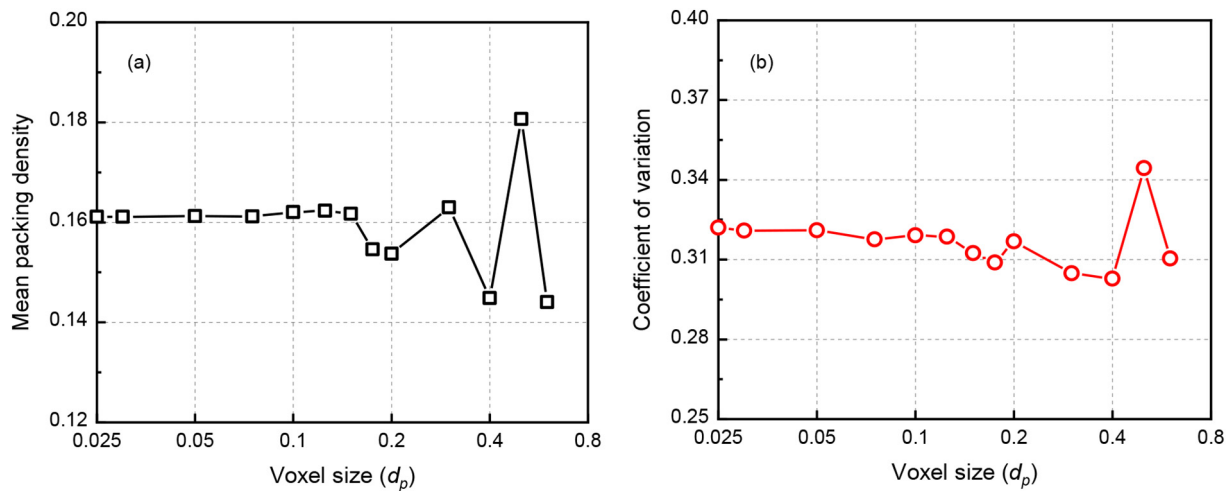
Fig. 8. Effects of voxel size on (a) average packing density and (b) coefficient of variation of local packing density.

difference smaller than 0.2%. A decrease in the mean packing density can be observed when the grid size is larger than $2.5d_p$, resulting in a relative difference of 0.72% between $3.0d_p$ and $0.25d_p$. A grid size smaller than 2/3 of the sampling size is thus recommended to give a statistically more consistent result. In contrast, there is no lower bound of grid size as it is only limited by the available memory space.

4.1.3. Effect of voxel size

Voxel size affects both the accuracy of sampled local packing density and the computational cost. It is thus worthwhile to determine the maximum allowable voxel size which can provide an acceptable accuracy. A range of voxel sizes are examined here while keeping both the local sampling size (i.e. $3.0d_p$) and the grid size (i.e. $1.0d_p$) constant. As shown in Fig. 8(a), little variation is observed in the mean value of packing density up to a voxel size of $0.15d_p$, with a relative difference within 0.1%. The same conclusion can also be drawn for the coefficient of variation of packing density, as shown in Fig. 8(b), which remains relatively stable up to a voxel size of $0.15d_p$ beyond which significant variation can be observed. A voxel size smaller than $0.15d_p$ is thus recommend for a statistically stable sampling of packing density.

4.2. Surface profile

Surface uniformity of a spread powder layer can be assessed from its surface profile. Local surface height is calculated as the maximum surface height within the local sampling area. If no particle is found within this sampling area, the surface height is then taken as zero. Consequently, the smaller the local sampling size, the smaller the empty patch that can be identified. However, this does not mean a sampling head of vanishing size should be used. A head of a finite thickness (larger than particle diameter) is required to isolate the effects of packing density and surface roughness of the powder layer to provide a pure surface characterisation [9]. Here, the effect of local sampling size on the resulting surface profile is examined. As shown in Fig. 9(a), the surface height varies from 0 to $1.5d_p$. Sampling size shows a significant impact on the resulting surface profile, with a larger sampling size showing a better surface homogeneity. The blue-coloured region indicates the presence of local empty patches, which reduces with increasing sampling size. This can also be confirmed from Fig. 9(b) which shows the frequency distributions of surface height. Two significant peaks can be observed at 0 and $1.0d_p$, indicating a dominant mono-layered packing structure. The frequency of surface height decreases with sampling size for a surface height smaller than $0.75d_p$ while increases with it for
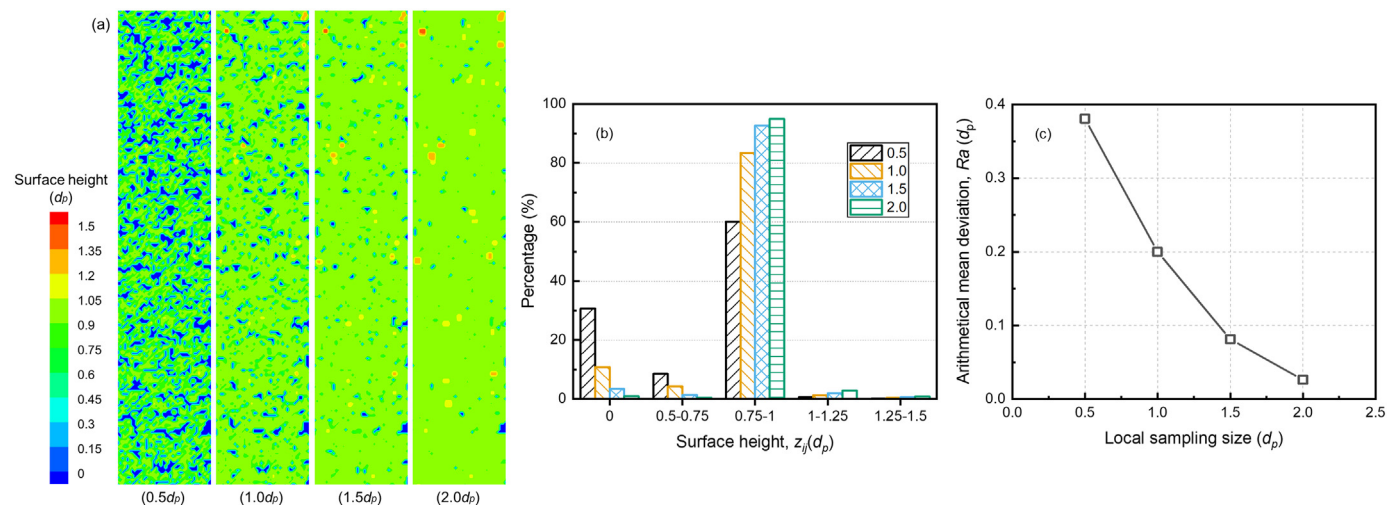
Fig. 9. Effect of local sampling size on (a) surface profile (colour codes refer to surface height), (b) distribution of surface height and (c) surface roughness of spread powder layer. The surface height is normalised by the particle diameter.

those larger than $0.75d_p$, corresponding to a decreasing surface roughness as shown in Fig. 9(c). To retain the information of both local empty patches and the dominant layer thickness, the local sampling size should then be selected between $1.0d_p$ and $1.5d_p$.

4.3. Density pore

4.3.1. Effect of local sampling size

Fig. 10(a) shows the spatial distribution of density pores obtained by thresholding contour maps of local packing density with a value of 0.1, where each pore is coloured by its orientation relative to the spreading direction. Here, four different local sampling sizes are used to calculate local packing density while keeping voxel size and sampling grid size constant as $0.05d_p$ and $0.1d_p$, respectively. As discussed before (i.e. Section 2.1.1), a large sampling size tends to smooth out variation of local packing density. A large sampling size would therefore reduce pore size, leading to a reduced number of pores that can be identified. Fig. 10 (b) shows the cumulative distributions of pore size. Here, the pore size is defined as its equivalent circular area diameter of the pore. Decreasing sampling size leads to enlarged size range of pores that can be identified. However, the sampling size has little influence on the variability of pore size, as the coefficient of variation remains relatively stable around 0.87.

As shown in Fig. 10(c), most of the pores are found to align either close to the spreading direction or in the direction perpendicular to it. The proportion of pores aligned in these two directions increases slightly with sampling size, indicating those small pores identified by a small sampling size tend to have random orientations. The circularity of pores also increases slightly with increasing sampling size, suggesting pores identified by a large sampling size tend to have a round shape.

4.3.2. Effect of density threshold

Another important parameter affecting the sampling of density pores is the density threshold. Four different threshold values are tested here: 0.06, 0.08, 0.1 and 0.12. Spatial distributions of the resulting density pores are shown in Fig. 11(a), where the pore size is seen to increase with the density threshold while the number of pores remains almost constant. The cumulative pore size distribution in Fig. 11(b) follows a similar trend for small pores but results in a total pore coverage increasing with density threshold. On the other hand, the orientation of density pores in Fig. 11(c) shows little dependence on the density threshold, with orientations either close to the spreading direction or in the direction perpendicular to that. The shape of pores is slightly affected, as shown in Fig. 11(d). The average circularity decreases with density threshold, indicating an increased irregularity of the pore shape. Two
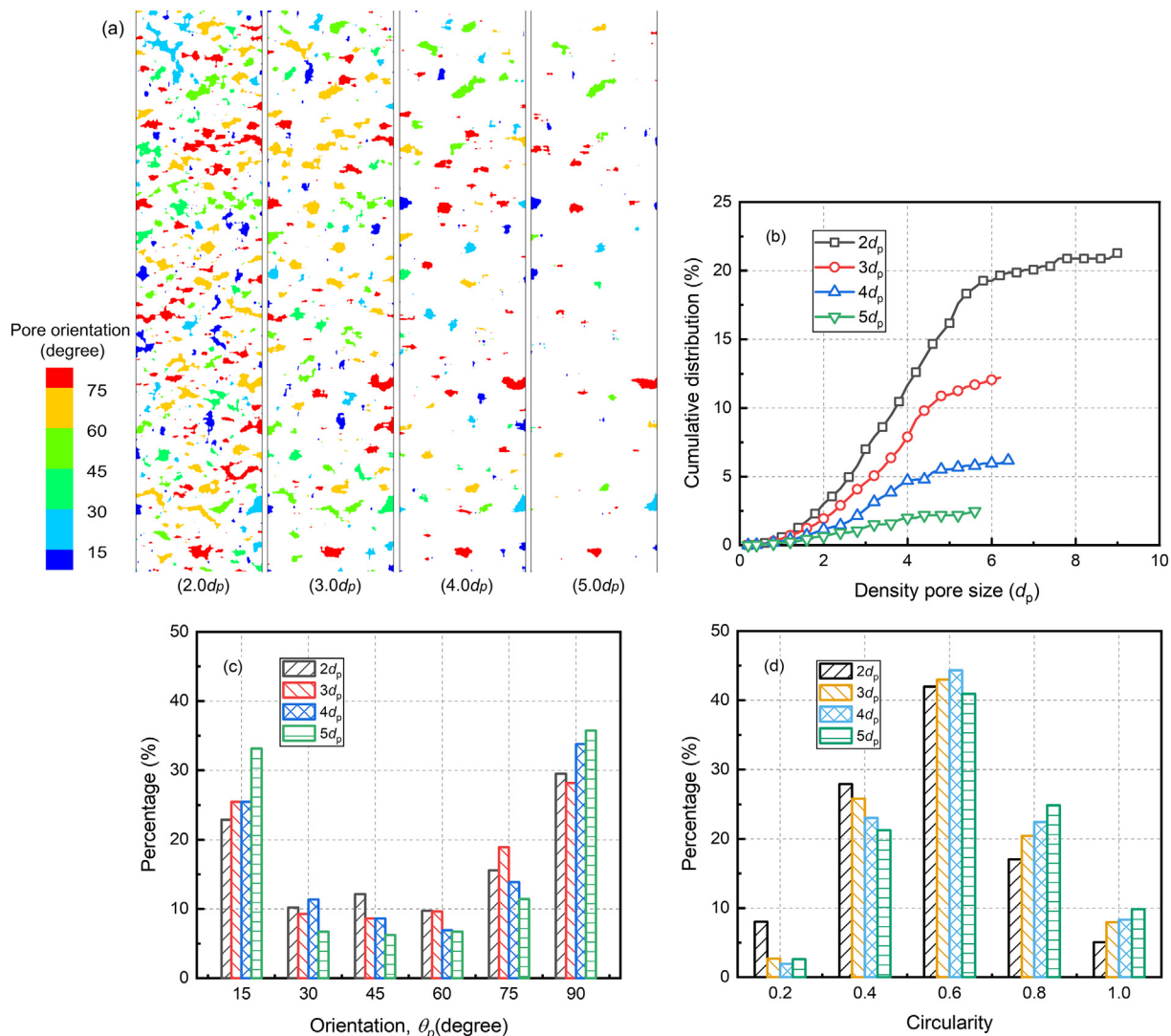
Fig. 10. (a) Spatial distribution of the density pore calculated by different sampling sizes, where each pore is coloured by its angle relative to the spreading direction and effect of sampling size on (b) cumulative pore size distribution, (c) orientation and (d) circularity of density pores.
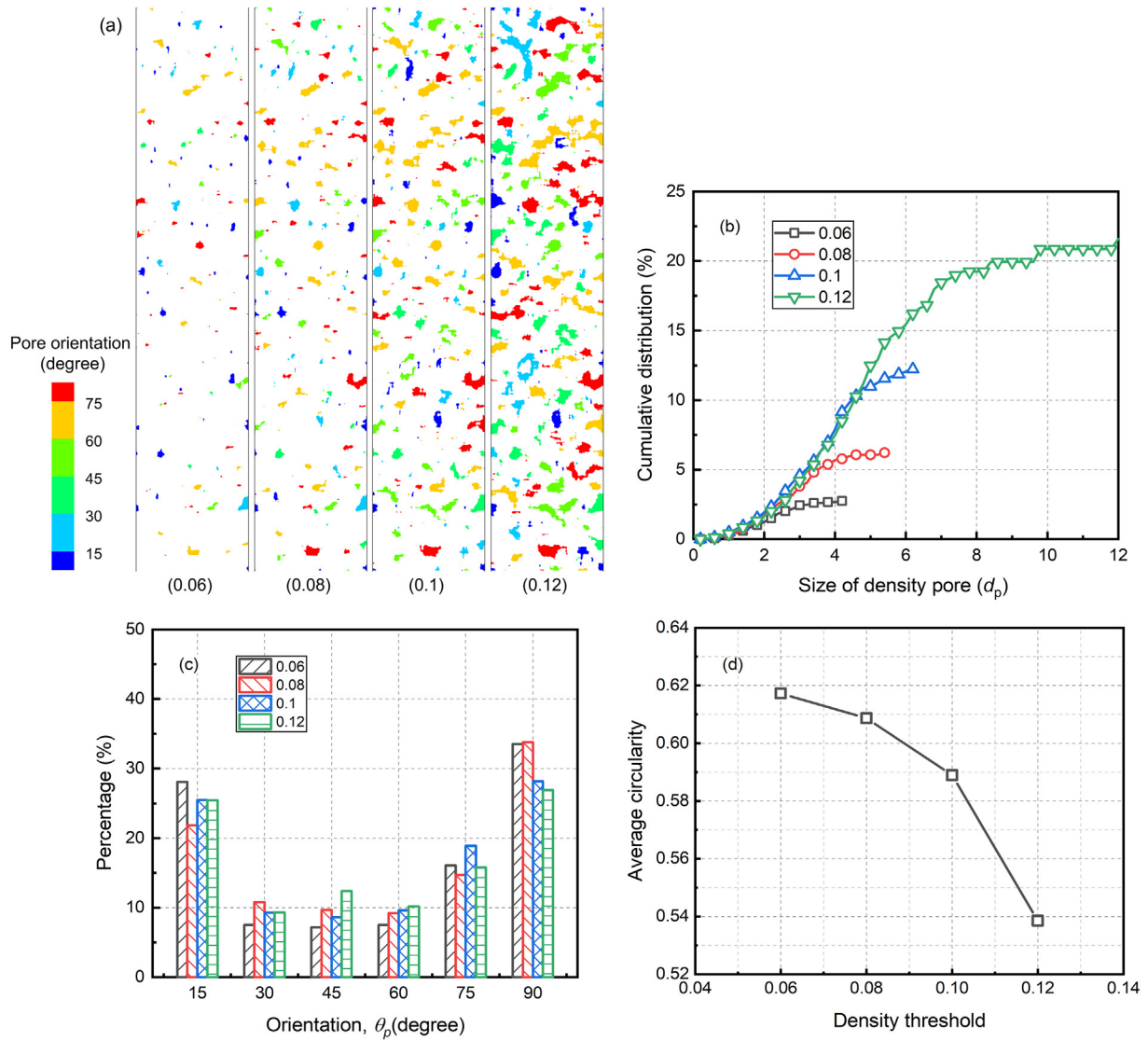
Fig. 11. (a) Spatial distribution of density pores calculated by different density thresholds, where each pore is coloured by its angle relative to the spreading direction and effect of density threshold on (b) cumulative pore size distribution, (c) orientation and (d) average circularity of density pores.
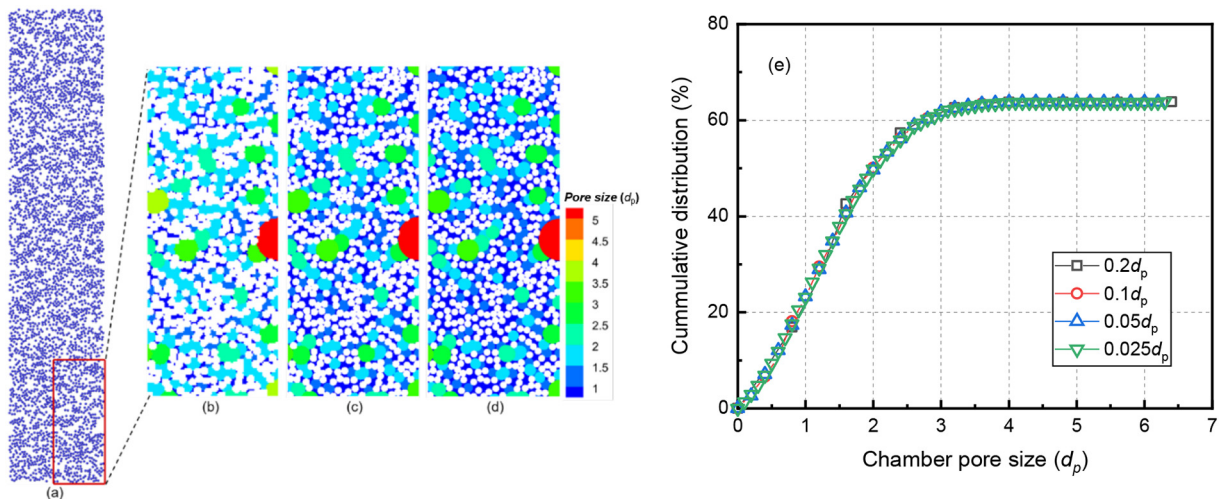
Fig. 12. (a) top view of the spread powder bed and chamber pores identified by different pixel sizes of (b) $0.2d_p$, (c) $0.1d_p$ and (d) $0.05d_p$. (e) Effect of pixel size on the cumulative size distribution of chamber pores.

Table 6
Summary of results obtained from G3 morphologi for Ti-6Al-4 V particles.

CE diameter mean (μm)	HS circularity mean	Aspect ratio mean	Elongation mean	Solidity mean
49.16	0.979	0.96	0.04	0.996

possible causes for the change of density pores can be proposed: the pores identified by a small threshold value can either be enlarged without much change in its shape or two isolated pores can be merged to form a larger pore with an elongated shape, consequently leading to the increase of pore size and decrease of circularity.

4.4. Chamber pore

The spatial and cumulative size distributions of sampled chamber pores are shown in Fig. 12, where four different pixel sizes are tested: $0.1d_p$, $0.05d_p$, $0.025d_p$ and $0.0125d_p$. Both results show that sampling of chamber pores are largely insensitive to the pixel sizes. The cumulative size distributions of different pixel sizes follow the same trend, reaching a total coverage around 63.8%. Although pixel size determines the smallest size of chamber pores that can be identified, roughly same largest size of chamber pores (i.e. $6.3d_p$) is obtained for all the cases, indicating a pixel size smaller than $0.1d_p$ is sufficient to obtain consistent results.

5. Application to experimentally characterised spread bed

The developed approach is further applied to experimentally spread powder layers. Plasma atomised Ti-6Al-4V powder was tested in a recently developed rig to replicate the spreading process in AM machine. The properties of the as-received powder were measured as follows: A cold field emission scanning electron microscope (CFE-SEM, Hitachi SU8230, LEMAS) operated at 10 kV was used to examine the morphology of particles. Size distribution of particles was measured using a laser diffraction analyser (Malvern Mastersizer 2000, UK) according to the standard method (ASTM B822–17). The powder was tested using the dry dispersion method and the average values of D_{10}, D_{50} and D_{90}

for five runs were reported. The G3 morphologi particle characterisation system (Malvern Panalytical Ltd., UK) was also used to measure shape distribution of Ti64 particles. 5 mm³ of particles were placed into the dispersion capsule and particles were evenly dispersed over a glass plate using high-pressure (5 bar) with pressure pulse injection time of 20 ms. Optical microscope of 5× (6.5–420 μm) magnification was then used to analyse the particles. The mean particle diameter, circularity, aspect ratio, elongation, and solidity values based on 22,959 particles covered within projected scan area are shown in Table 6. Fig. 13 shows the particle size distribution and morphology of the Ti-6Al-4 V powder, indicating a highly spherical particle shape.

The powder was spread over a flat substrate using a rig blade, with a speed of 50 mm/s and a blade gap of D_{90} (i.e. 50 μm) of the tested powder. Herein, the focus is given to the applicability of the developed characterisation approach. It should be mentioned that, packing density and chamber pore size can be extracted quite accurately by the present approach. However, surface profiles are difficult to obtain as the optical images lacks the information in the vertical direction and thus are not shown here. The experiments were repeated nine times and the resulting information is summarised below.

Images of the spread powder bed is taken by a high-speed camera after spreading and are stitched together to form a larger image (Fig. 14(a)). The locations and sizes of the particles are extracted from the stitched image using a MATLAB code, by which most of the particles (>99%) can be identified (Fig. 14(b)). A numerical counterpart of the spread powder bed is created using the extracted particle coordinates and sizes, as shown in Fig. 14(c). The developed characterisation approach is then applied to extract the structural information. To discretise the computational domain, a voxel size of $0.05D_{min}$ is used. Density is sampled using a sampling size of $3.0D_{90}$ on a sampling grid with a grid size of $0.5D_{90}$. Fig. 14(d) shows the resulting spatial distributions of packing density for four different runs, showing non-uniform density distribution along the spreading direction. The distribution of packing density is averaged over nine runs of the spreading. The sampling height for the packing density is set to the largest particle diameter. The resulting probability distribution is shown in Fig. 14(e). The averaged distribution of packing density follows a Gaussian distribution, with a mode of 0.214.

Fig. 15 shows the process of identifying chamber pores from the image of the spread powder bed. Only a section of the image is shown
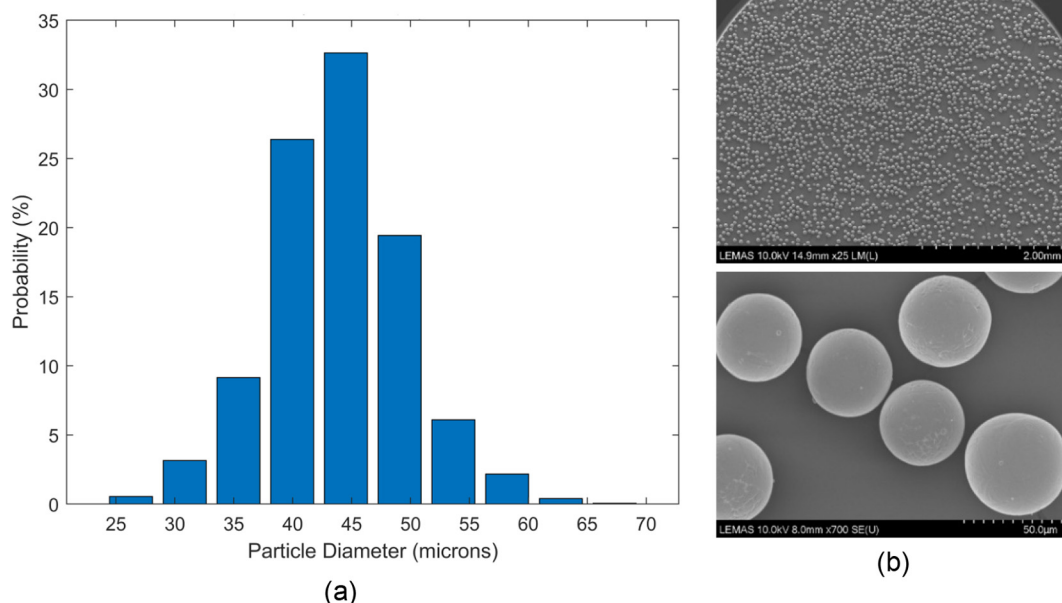
Fig. 13. (a) Particle size distribution of the plasma atomised Ti-6Al-4 V powder used for spreading and (b) SEM images of the Ti-6Al-4 V powder under different magnification.
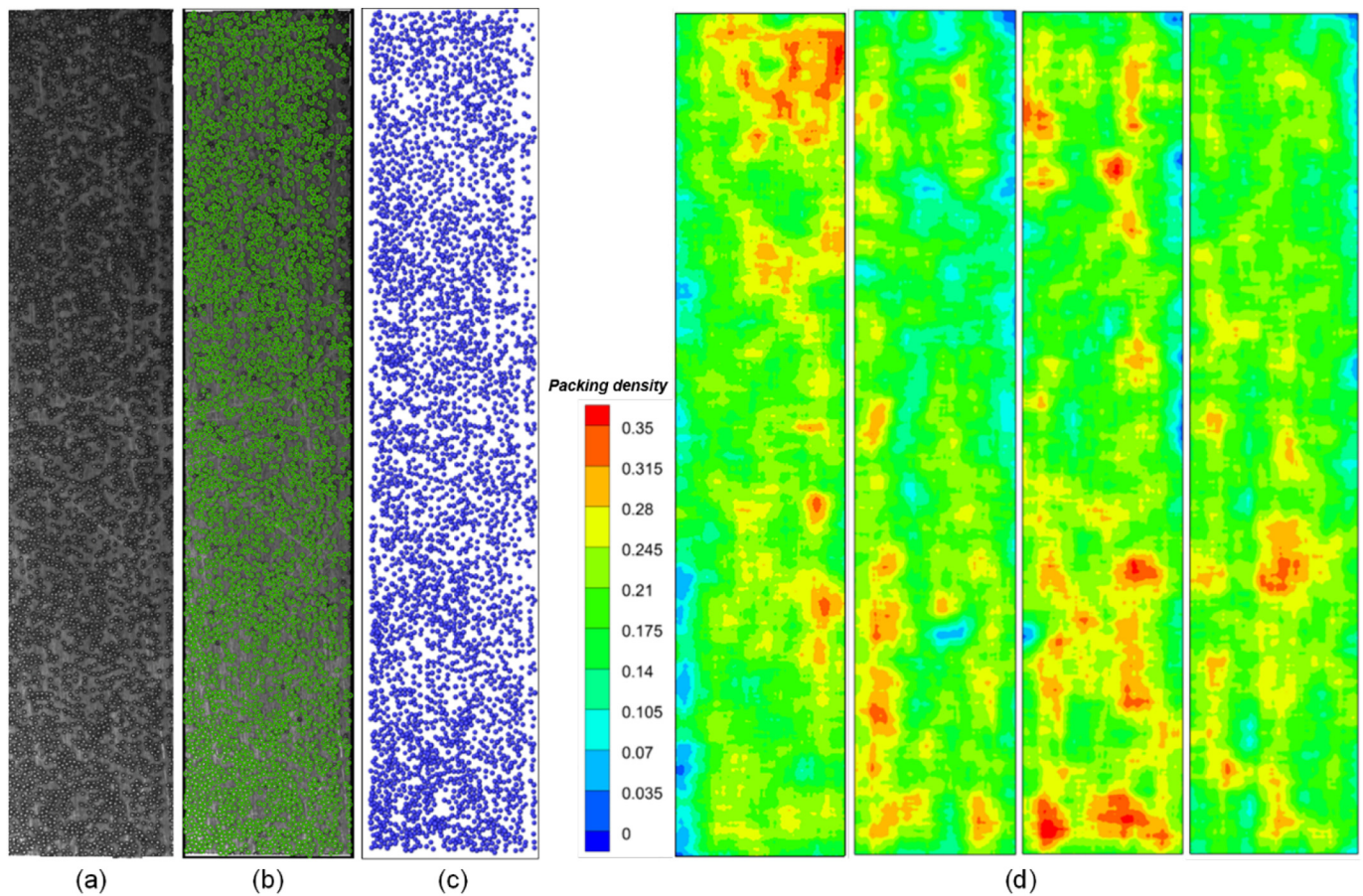
Fig. 14. (a) Stitched image from high speed camera, (b) particle size and locations extracted by a MATLAB code, (c) re-created spread powder bed, (d) contour map of packing density for four different runs, in which the first one corresponds to the particle distribution shown in (a), (e) distribution of local packing density in the spread powder bed. The solid line is the Gaussian fitting.

here as an example (Fig. 15(a)). To discretise the image, a pixel size of $0.1D_{90}$ is used. The particles are first projected on the substrate surface. The resulted projection is shown in Fig. 15(b), where a solid pixel is represented in red while an empty pixel is shown in blue. The identified chamber pores are shown in Fig. 15(c). Chamber pores larger than the particle size can be observed, which distributes quite randomly
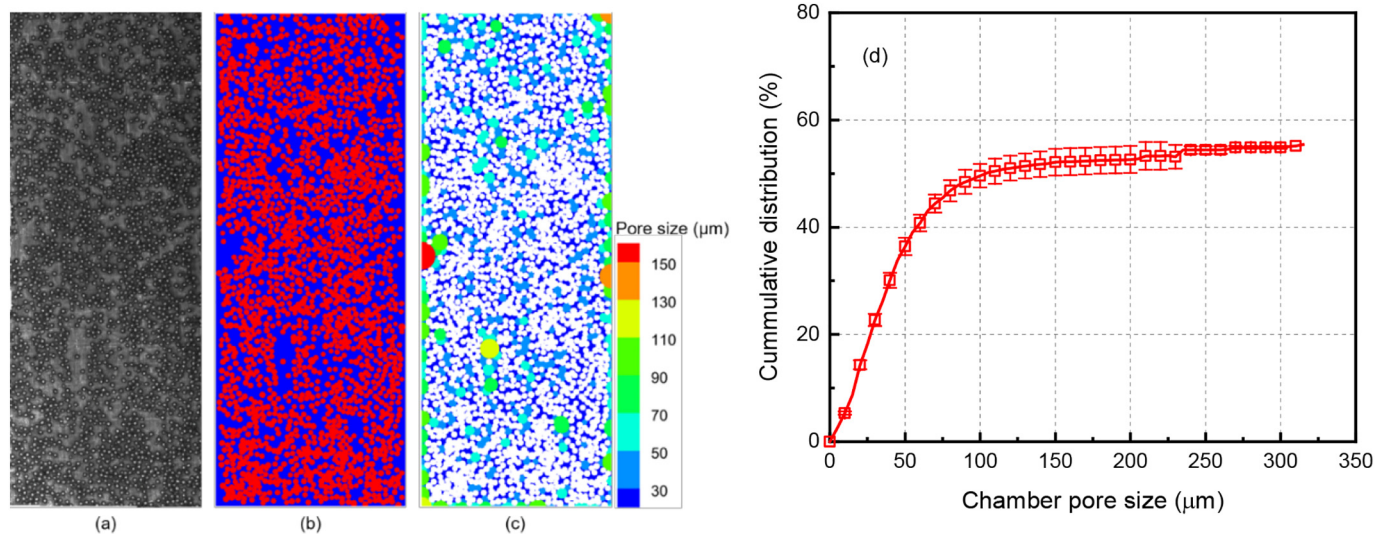
Fig. 15. (a) A section of the spread powder bed captured in the experiment, (b) identification of solid and empty pixels, (c) identification of chamber pores and (d) cumulative size distribution of chamber pores.

throughout the spread powder bed. Fig. 15(d) shows the cumulative size distribution of chamber pores. The results are averaged over nine runs, which gives a total pore coverage around 53.5% of the whole spreading powder bed.

6. Conclusions

In the present study, a digital-based approach has been proposed for the characterisation of a spread powder layer. It is based on the spatial discretisation of the working space, from which the packing density, surface profile and pore characteristics can be evaluated. A so-called density pore is proposed to identify the less populated regions in the spread powder bed by thresholding the contour map of local packing density. The density pore can then be characterised in terms of size, shape, and orientation. The chamber pores are defined based on the projection of particles onto the substrate, from which the size distribution of the empty patches can be quantified. Combined with imaging analysis, this approach is demonstrated to be useful for extracting structural information from both DEM modelled and experimentally spread powder layers. Sensitivity analysis on the sampling parameters has also been conducted, leading to the following findings,

• Sampling of packing density depends on the local sampling size. A large sampling size tends to smooth out local gradient, leading to a reduced coefficient variation but without much influence on the mode of the density distribution. A voxel size smaller than $0.15d_p$ and a sampling grid size smaller than 2/3 of the local sampling size are suggested to give statistically consistent and stable sampling of the packing density.
• Both local sampling size and density threshold can affect the sampling of density pores. Decreasing local sampling size increases the size range of pores that can be identified, without much effect on the variability of the size of density pore, An increase in density threshold leads to an enlarged size range, a more irregular pore shape while not changing much of the number of pores.
• The sampling of chamber pores is largely insensitive to pixel size. The pixel size mainly determines the smallest size of pores that can be identified. A pixel size smaller than $0.1d_p$ is recommended.

This approach is generally applicable to spread powder layers consisting of particles with varying sizes and non-spherical shapes, which not only provides a solid basis for quantitative evaluation of powder spreadability but also enriches the structural analysis of a spread

powder layer. Application of this approach for the calibration and validation of DEM modelling will be reported in the near future.

Data availability

Representative samples of the research data are given in the figures and tables. Other datasets generated and/or analysed during this study are not publicly available due to their large size but are available from the corresponding author upon reasonable request.

CRediT authorship contribution statement

Yi He: Conceptualization, Methodology, Software, Investigation, Validation, Formal analysis, Visualization, Writing - original draft, Writing - review & editing. **Jabbar Gardy:** Writing - review & editing, Formal analysis (Experiment & Matlab image analysis). **Ali Hassanpour:** Writing - review & editing. **Andrew E. Bayly:** Writing - review & editing, Investigation, Funding acquisition.

Declaration of Competing Interest

The authors declare that they have no known competing financial interests or personal relationships that could have appeared to influence the work reported in this paper.

References

[1] J. Parthasarathy, B. Starly, S. Raman, A design for the additive manufacture of functionally graded porous structures with tailored mechanical properties for biomedical applications, J. Manuf. Process. 13 (2011) 160–170, https://doi.org/10.1016/j.jmapro.2011.01.004.
[2] W.J. Sames, F.A. List, S. Pannala, R.R. Dehoff, S.S. Babu, The metallurgy and processing science of metal additive manufacturing, Int. Mater. Rev. 61 (2016) 315–360, https://doi.org/10.1080/09506608.2015.1116649.

[3] J.H. Tan, W.L.E. Wong, K.W. Dalgarno, An overview of powder granulometry on feedstock and part performance in the selective laser melting process, Addit. Manuf. 18 (2017) 228–255, https://doi.org/10.1016/j.addma.2017.10.011.

[4] Z. Zhu, S. Lou, C. Majewski, Characterisation and correlation of areal surface texture with processing parameters and porosity of high speed sintered parts, Addit. Manuf. 36 (2020) 101402, https://doi.org/10.1016/j.addma.2020.101402.

[5] S. Ziegelmeier, P. Christou, F. Wöllecke, C. Tuck, R. Goodridge, R. Hague, E. Krampe, E. Wintermantel, An experimental study into the effects of bulk and flow behaviour of laser sintering polymer powders on resulting part properties, J. Mater. Process. Technol. 215 (2015) 239–250, https://doi.org/10.1016/j.jmatprotec.2014.07.029.

[6] D. Sofia, D. Barletta, M. Poletto, Laser sintering process of ceramic powders: the effect of particle size on the mechanical properties of sintered layers, Addit. Manuf. 23 (2018) 215–224, https://doi.org/10.1016/j.addma.2018.08.012.

[7] S.E. Brika, M. Letenneur, C.A. Dion, V. Brailovski, Influence of particle morphology and size distribution on the powder flowability and laser powder bed fusion manufacturability of Ti-6Al-4V alloy, Addit. Manuf. 31 (2020) 100929, https://doi.org/10.1016/j.addma.2019.100929.

[8] W. Nan, M. Pasha, T. Bonakdar, A. Lopez, U. Zafar, S. Nadimi, M. Ghadiri, Jamming during particle spreading in additive manufacturing, Powder Technol. 338 (2018) 253–262, https://doi.org/10.1016/j.powtec.2018.07.030.

[9] C. Meier, R. Weissbach, J. Weinberg, W.A. Wall, A.J. Hart, Critical influences of particle size and adhesion on the powder layer uniformity in metal additive manufacturing, J. Mater. Process. Technol. 266 (2019) 484–501, https://doi.org/10.1016/j.jmatprotec.2018.10.037.

[10] H. Chen, Q. Wei, S. Wen, Z. Li, Y. Shi, Flow behavior of powder particles in layering process of selective laser melting: numerical modeling and experimental verification based on discrete element method, Int. J. Mach. Tools Manuf. 123 (2017) 146–159, https://doi.org/10.1016/j.ijmachtools.2017.08.004.

[11] H. Chen, Q. Wei, Y. Zhang, F. Chen, Y. Shi, W. Yan, Powder-spreading mechanisms in powder-bed-based additive manufacturing : experiments and computational modeling, Acta Mater. 179 (2019) 158–171, https://doi.org/10.1016/j.actamat.2019.08.030.

[12] H. Chen, Y. Chen, Y. Liu, Q. Wei, Y. Shi, W. Yan, Packing quality of powder layer during counter-rolling-type powder spreading process in additive manufacturing, Int. J. Mach. Tools Manuf. 153 (2020) 103553, https://doi.org/10.1016/j.ijmachtools.2020.103553.

[13] S. Haeri, Y. Wang, O. Ghita, J. Sun, Discrete element simulation and experimental study of powder spreading process in additive manufacturing, Powder Technol. 306 (2017) 45–54, https://doi.org/10.1016/j.powtec.2016.11.002.

[14] L. Wang, E.L. Li, H. Shen, R.P. Zou, A.B. Yu, Z.Y. Zhou, Adhesion effects on spreading of metal powders in selective laser melting, Powder Technol. 363 (2020) 602–610, https://doi.org/10.1016/j.powtec.2019.12.048.

[15] Y.M. Fouda, A.E. Bayly, A DEM study of powder spreading in additive layer manufacturing, Granul. Matter 22 (2020) 1–18, https://doi.org/10.1007/s10035-019-0971-x.

[16] L.I. Escano, N.D. Parab, L. Xiong, Q. Guo, C. Zhao, K. Fezzaa, W. Everhart, T. Sun, L. Chen, Revealing particle-scale powder spreading dynamics in powder-bed-based additive manufacturing process by high-speed X-ray imaging, Sci. Rep. 8 (2018) 1–11, https://doi.org/10.1038/s41598-018-33376-0.

[17] M. Ahmed, M. Pasha, W. Nan, M. Ghadiri, A simple method for assessing powder spreadability for additive manufacturing, Powder Technol. 367 (2020) 671–679, https://doi.org/10.1016/j.powtec.2020.04.033.

[18] D. Ruggi, M. Lupo, D. Sofia, C. Barrès, D. Barletta, M. Poletto, Flow properties of polymeric powders for selective laser sintering, Powder Technol. 370 (2020) 288–297, https://doi.org/10.1016/j.powtec.2020.05.069.

[19] A. Baule, R. Mari, L. Bo, L. Portal, H.A. Makse, Mean-field theory of random close packings of axisymmetric particles, Nat. Commun. 4 (2013) 1–11, https://doi.org/10.1038/ncomms3194.

[20] K.A. Newhall, I. Jorjadze, E. Vanden-Eijnden, J. Brujic, A statistical mechanics framework captures the packing of monodisperse particles, Soft Matter 7 (2011) 11518–11525, https://doi.org/10.1039/c1sm06243c.

[21] M. Suzuki, T. Shinmura, K. Iimura, M. Hirota, Study of the wall effect on particle packing structure using X-ray micro computed tomography, Adv. Powder Technol. 19 (2008) 183–195, https://doi.org/10.1163/156855208X293817.

[22] W. Zhang, K.E. Thompson, A.H. Reed, L. Beenken, Relationship between packing structure and porosity in fixed beds of equilateral cylindrical particles, Chem. Eng. Sci. 61 (2006) 8060–8074, https://doi.org/10.1016/j.ces.2006.09.036.

[23] R.Y. Yang, R.P. Zou, A.B. Yu, Computer simulation of the packing of fine particles, Phys. Rev. E 62 (2000) 3900–3908, https://doi.org/10.1103/PhysRevE.62.3900.

[24] R.Y. Yang, R.P. Zou, A.B. Yu, Voronoi tessellation of the packing of fine uniform spheres, Phys. Rev. E 65 (2002), 041302, https://doi.org/10.1103/PhysRevE.65.041302.

[25] K. Dong, C. Wang, A. Yu, Voronoi analysis of the packings of non-spherical particles, Chem. Eng. Sci. 153 (2016) 330–343, https://doi.org/10.1016/j.ces.2016.07.013.

[26] M. Clusel, E.I. Corwin, A.O.N. Siemens, J. Bruji, A granocentric model for random packing of jammed emulsions, Nature 460 (2009) 611–615, https://doi.org/10.1038/nature08158.

[27] C. Song, P. Wang, H.A. Makse, A phase diagram for jammed matter, Nature. 453 (2008) 629–632, https://doi.org/10.1038/nature06981.

[28] E.I. Corwin, M. Clusel, A.O.N. Siemens, J. Brujić, Model for random packing of polydisperse frictionless spheres, Soft Matter 6 (2010) 2949–2959, https://doi.org/10.1039/c000984a.

[29] W. Liu, S. Li, A. Baule, H.A. Makse, Adhesive loose packings of small dry particles, Soft Matter 11 (2015) 6492–6498, https://doi.org/10.1039/c5sm01169h.

[30] W. Nan, M. Pasha, M. Ghadiri, Numerical simulation of particle flow and segregation during roller spreading process in additive manufacturing, Powder Technol. 364 (2020) 811–821, https://doi.org/10.1016/j.powtec.2019.12.023.

[31] S. Haeri, Optimisation of blade type spreaders for powder bed preparation in additive manufacturing using DEM simulations, Powder Technol. 321 (2017) 94–104, https://doi.org/10.1016/j.powtec.2017.08.011.

[32] W. Nan, M. Pasha, M. Ghadiri, Effect of gas-particle interaction on roller spreading process in additive manufacturing, Powder Technol. 372 (2020) 466–476, https://doi.org/10.1016/j.powtec.2020.05.119.

[33] H. Chen, W. Yan, Spattering and denudation in laser powder bed fusion process: multiphase flow modelling, Acta Mater. 196 (2020) 154–167, https://doi.org/10.1016/j.actamat.2020.06.033.

[34] S.M. Sweeney, C.L. Martin, Pore size distributions calculated from 3-D images of DEM-simulated powder compacts, Acta Mater. 51 (2003) 3635–3649, https://doi.org/10.1016/S1359-6454(03)00183-6.

[35] Y. He, A. Hassanpour, M.A. Behjani, A.E. Bayly, A novel stiffness scaling methodology for discrete element modelling of cohesive fine powders, Appl. Math. Model. (2020).

[36] Y. He, T.J. Evans, A.B. Yu, R.Y. Yang, A GPU-based DEM for modelling large scale powder compaction with wide size distributions, Powder Technol. 333 (2018) 219–228, https://doi.org/10.1016/j.powtec.2018.04.034.

[37] Y. He, T.J. Evans, Y.S. Shen, A.B. Yu, R.Y. Yang, Discrete modelling of the compaction of non-spherical particles using a multi-sphere approach, Miner. Eng. 117 (2018) 108–116, https://doi.org/10.1016/j.mineng.2017.12.013.

[38] Y. He, Y.Y. Li, T.J. Evans, A.B. Yu, R.Y. Yang, Effects of particle characteristics and consolidation pressure on the compaction of non-spherical particles, Miner. Eng. 137 (2019) 241–249, https://doi.org/10.1016/j.mineng.2019.04.007.

[39] R.D. Mindlin, H. Deresiewicz, Elastic spheres in contact under varying oblique forces, ASME J. Appl. Mech. 20 (1953) 327–344.

[40] H.C. Hamaker, The London-van der Waals attraction between spherical particles, Physica 4 (1937) 1058–1072, https://doi.org/10.1016/S0031-8914(37)80203-7.

[41] Y. He, A.E. Bayly, A. Hassanpour, F. Muller, K. Wu, D. Yang, A GPU-based coupled SPH-DEM method for particle-fluid flow with free surfaces, Powder Technol. 338 (2018) 548–562, https://doi.org/10.1016/j.powtec.2018.07.043.

[42] Y. He, F. Muller, A. Hassanpour, A.E. Bayly, A CPU-GPU cross-platform coupled CFD-DEM approach for complex particle-fluid flows, Chem. Eng. Sci. 115712 (2020) https://doi.org/10.1016/j.ces.2020.115712.

[43] E.J.R. Parteli, T. Pöschel, Particle-based simulation of powder application in additive manufacturing, Powder Technol. 288 (2016) 96–102, https://doi.org/10.1016/j.powtec.2015.10.035.